

## Research article

# Selective capture of Pb(II) from aqueous solution by mercapto functionalized zirconium-based metal organic frameworks



Lejie Zhu<sup>a,b,1</sup>, Qiong Ouyang<sup>d,2</sup>, Donghao Liu<sup>b,1</sup>, Jian Zhu<sup>a,3</sup>, Yu Zhang<sup>a,3</sup>, Jiaqiuzi Zhang<sup>b,1</sup>, Kaiyin Shao<sup>b,1</sup>, Chengshuai Liu<sup>c,d,2,\*</sup>

<sup>a</sup> School of Resources and Environmental Engineering, Guizhou University, Guiyang, 550025, Guizhou, PR China

<sup>b</sup> School of Chemistry and Civil Engineering, Shaoguan University, Shaoguan, 512005, Guangdong, PR China

<sup>c</sup> Institute of Geochemistry, Chinese Academy of Sciences, Guiyang, 550025, Guizhou, PR China

<sup>d</sup> College of Natural Resources and Environment, South China Agricultural University, Guangzhou, 510000, Guangdong, PR China

## ARTICLE INFO

### Keywords:

Adsorption

Metal-organic frameworks

Surface modification

Lead removal

## ABSTRACT

UiO-66, a well-known metal-organic framework (MOF) with large surface area, modifiability, and high stability, has substantial potential for further advancements. In this study, UiO-66 is modified with thiocyanuric acid (TCA) and 2,5-dimercapto-1,3,4-thiadiazole (MTD) to prepare two high-sulfur-content adsorbents (UiO-66-TCA/MTD). Fourier-transform infrared spectroscopy (FT-IR), X-ray diffraction (XRD), and N<sub>2</sub> adsorption-desorption analysis show that the modified materials retain their crystal structure. Adsorption experiments demonstrate that UiO-66-TCA achieves a remarkable Pb(II) adsorption capacity of 967.66 mg/g, representing an 840 % enhancement over pristine UiO-66-NH<sub>2</sub>. The material exhibits exceptional selectivity, with separation factors reaching 2700.17 for Pb(II)/Mg(II) and 7967.20 for Pb(II)/Ba(II). X-ray photoelectron spectroscopy (XPS) and density functional theory (DFT) calculations confirm that the adsorption mechanism primarily involves surface coordination between sulfur elements in the modification layer and Pb(II), with mercapto groups as the key active sites. This study provides a theoretical basis for the design of sulfur-containing MOF materials and their application in lead-containing wastewater treatment.

## 1. Introduction

Heavy metal ions, such as lead, are significant contributors to global environmental pollution. The acceleration of industrialization and agricultural activities has markedly increased the accumulation of heavy metal ions. In developing countries, careless waste disposal and weak enforcement of environmental law regulations exacerbate heavy metal pollution (Baghayeri et al., 2018). Lead ions primarily enter water bodies through diffusion and, due to their non-biodegradable nature, persist in aquatic environments. Sulfur and nitrogen readily bind to lead ions, inducing harmful structural changes in proteins or enzyme inhibition (H. Liu et al., 2023). The accumulation of lead ions in the human body through the food chain poses substantial health risks, including nervous system damage, liver damage, and kidney damage (Akinterinwa et al., 2022; Al-Akeel et al., 2021; Kypritidou et al., 2022; Zhou et al.,

2020).

To address the issue of lead contamination in water, various methods have been employed, including chemical precipitation (Qiu et al., 2022), electrodialysis (Li et al., 2022), ion exchange (Sgreccia et al., 2024) and membrane separation (He et al., 2020; Youness et al., 2022). Although chemical precipitation is widely used in industrial contexts due to its simplicity and efficacy, it is associated with significant drawbacks, including secondary pollution and inefficient resource recovery (Zhu et al., 2018). Meanwhile, electrodialysis and membrane separation still face persistent challenges related to cost, efficiency, and safety (Wang et al., 2015).

In contrast, adsorption offers several distinct advantages, such as operational simplicity, rapid processing, and minimal secondary pollution, making it a preferred method for lead removal (Bai et al., 2024; Chen et al., 2022; Mahmood et al., 2024). A variety of adsorbents,

\* Corresponding author. College of Natural Resources and Environment, South China Agricultural University, Guangzhou, 510000, Guangdong, PR China.  
E-mail address: [csliu@scau.edu.cn](mailto:csliu@scau.edu.cn) (C. Liu).

<sup>1</sup> Present/Permanent Address: School of Chemistry and Civil Engineering, Shaoguan University, Shaoguan 512,005, Guangdong, PR China.

<sup>2</sup> Present/Permanent Address: College of Natural Resources and Environment, South China Agricultural University, Guangzhou 510,000, Guangdong, PR China.

<sup>3</sup> Present/Permanent Address: School of Resources and Environmental Engineering, Guizhou University, Guiyang 550,025, Guizhou, PR China.

including activated carbon (Albrektiene-Placake et al., 2023; Lach and Okoniewska, 2024), graphene oxide (Baghayeri et al., 2019), biomass (Al-Janabi et al., 2023; Gatabi et al., 2020; Lv et al., 2019), molecular sieves (Cui et al., 2024), and polymers (Maleki et al., 2019; Xie et al., 2024), have been employed in the process of lead removal. However, these adsorbents frequently exhibit limitations. Activated carbon exhibits moderate lead adsorption capacities, but suffers from poor selectivity, while biomass-based adsorbents offer low-cost alternatives but with limited adsorption capacity, insufficient selectivity, and challenges in reusability (Chowdhury et al., 2022; Ismail et al., 2023).

Among the various adsorbents available, metal organic frameworks (MOFs) are particularly notable for their efficacy. MOFs possess significant advantages, including high porosity, large specific surface area, and facile modifiability, which contribute to their widespread use in adsorbing heavy metal ions and organic compounds (Abdollahi et al., 2020; Alivand et al., 2021). However, MOFs are characterized by structural complexity and often exhibit limited stability in aqueous environments, particularly when the organic ligands are coordinated with low-valent metal ions such as Co(II), Zn(II), and Cu(II). In contrast, MOFs with high-valent metal ions such as Zr(IV), Ce(IV), and Ti(IV) as the central ions generally demonstrate enhanced stability in aqueous environments (Molavi, 2025). The Zr-based MOF series, UiO-66, is regarded as a promising candidate for wastewater treatment applications. It exhibits several remarkable properties including high thermal stability, superior chemical resistance to multiple solvents, excellent stability under various conditions, and exceptional resistance to high external pressures. These attributes are primarily attributed to the robust Zr-O bonds and the high coordination number between the Zr clusters and organic ligands, which contribute to its numerous potential applications in wastewater treatment (Ahmadijokani et al., 2022). exhibits considerably enhanced chemical stability, with negligible decomposition in water and substantial resistance to both acidic and alkaline conditions. However, pristine UiO-66 possesses a limited number of adsorption sites, which restricts its adsorption capacity. To overcome this limitation, surface modification became a prominent focus in recent research (Liu et al., 2023). For instance, Yang et al. synthesized ethylenediaminetetraacetic acid (EDTA) modified UiO-66, designated as UiO-66-EDTA, by employing UiO-66-NH<sub>2</sub> and EDTA dianhydride, achieving a maximum Cu(II) adsorption capacity of 154.8 mg/g (Yang et al., 2023). Liu et al. functionalized the surface of UiO-66 using dodecane and polyethyleneimine for dye adsorption from aqueous solutions, the maximum adsorption capacities for Congo Red and Methylene Blue were 583.4 mg/g and 286.3 mg/g, respectively, indicating a high affinity and adsorption capacity for these dyes (Liu et al., 2024).

According to the Hard-Soft Acid-Base (HSAB) theory, Lewis acids and bases can be classified into three categories-hard, soft, and borderline-based on properties such as size, polarizability, and charge density. Mercapto group are characteristic soft bases due to its relatively large size, high polarizability, and the low electron density, making it particularly effective for coordinating with soft Lewis acids (He et al., 2024; Liu et al., 2024; Zhang et al., 2023). Although lead ion are classified as borderline acids, their exhibit dominant soft-acid behavior in practice. The coordination interaction between lead ions and mercapto groups such as cysteine is the main mechanism of lead toxicity (Martinez-Haro et al., 2011; Winiarska-Mieczan, 2018). It is therefore hypothesized that mercapto groups can form stable complexes with lead ions, where increasing thiol density enhances Pb(II) adsorption capacity. Motivated by these properties, TCA and MTD were functionalized onto the surface of UiO-66 to improve Pb(II) adsorption performance. The TCA containing three mercapto groups, and MTD with two, are highly effective Pb-chelating agents. These mercapto-containing agents provide strong adsorption sites for the Pb(II) ions from aqueous media.

In this study, Zr(IV) in UiO-66 were utilized to catalyze the acetal reaction between thiols and aldehydes enabling the covalent grafting of two high-thiol-content monomers, TCA and MTD, were successfully

loaded onto the surface of UiO-66-NH<sub>2</sub>. Resulting in the preparation of two novel thiol-modified MOFs, with the objective of improving the adsorption efficiency for lead ions in water. The new synthesized MOFs were characterized using a variety of analytical techniques. Their adsorption behavior, including adsorption kinetics, adsorption isotherm, adsorption thermodynamics, influence of pH, ions, and recycle capacity of Pb(II) adsorption, was systematically evaluated. The mechanisms underlying Pb(II) adsorption were comprehensively studied through various investigative methods such as energy dispersive spectrometer (EDS), mapping, XPS, zeta potential, and DFT calculations.

## 2. Experimental

### 2.1. Chemicals and materials

Zirconium chloride (ZrCl<sub>4</sub>, 99.9 % metal basis), 2-aminoterephthalic acid (ATA, 98 %), 2,5-dimercapto-1,3,4-thiadiazole (MTD, 97 %), Tri-thiocyanuric acid (TCA, 95 %) were purchased from Macklin. Pb(NO<sub>3</sub>)<sub>2</sub> (99.9 %) and ethanol (95 %) were obtained from Sinopharm Co., Ltd. N, N-dimethylformamide (DMF, AR), acetic acid, glutaraldehyde (50 % in H<sub>2</sub>O, AR), methanol (AR), hydrochloric acid (37 % in H<sub>2</sub>O, AR) nitric acid (AR, 65 %–68 %) and absolute ethanol were obtained from Tianjin Damao Chemical Reagent Factory. The above materials were directly applied without any further purification.

### 2.2. Synthesis procedures

#### 2.2.1. Synthesis of UiO-66-NH<sub>2</sub>

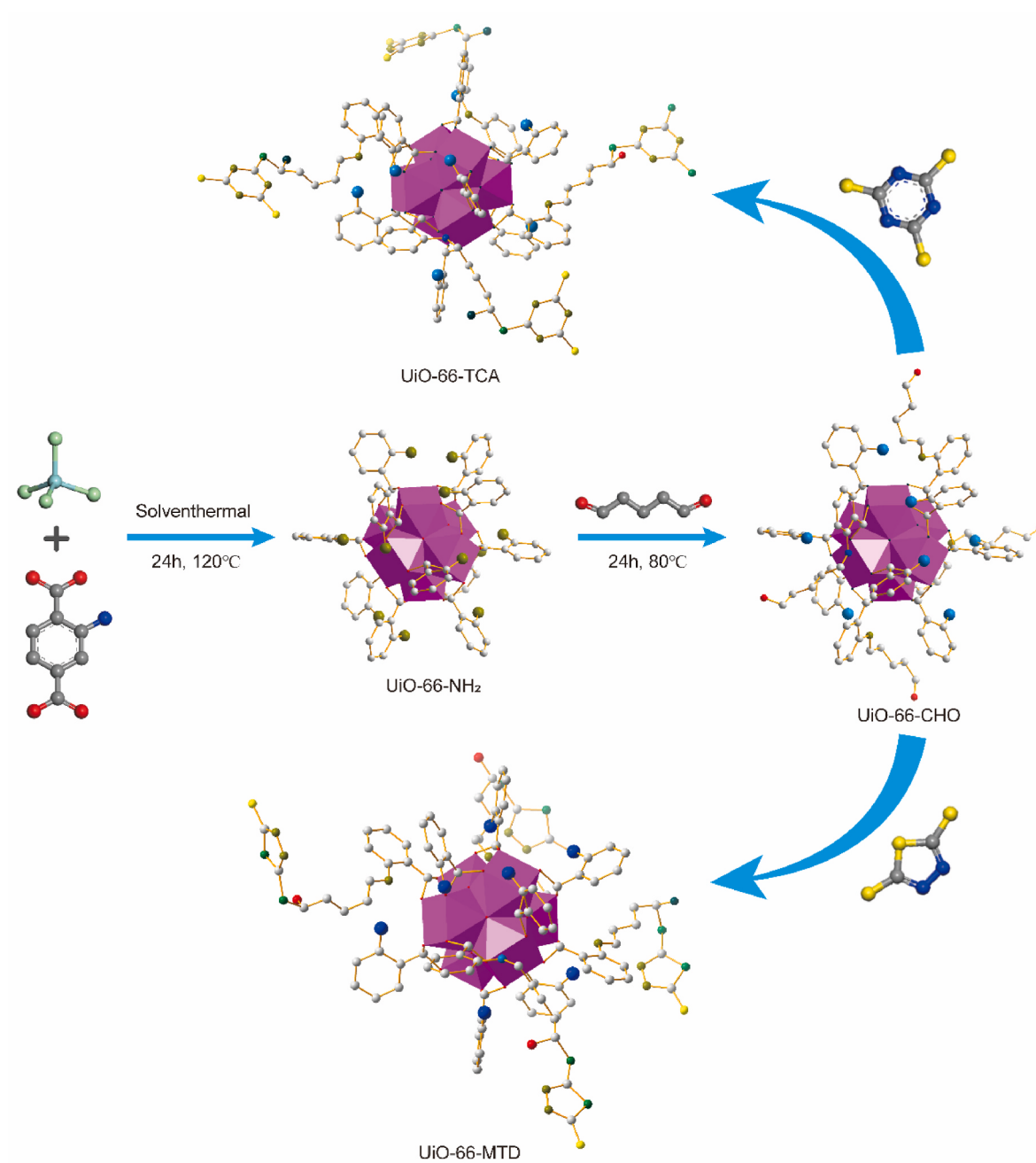
The original UiO-66-NH<sub>2</sub> was synthesized via a solvothermal method following a previous research (Zhao et al., 2020). Initially, 0.42g of ZrCl<sub>4</sub> and 0.45g of ATA were fully dissolved in 50 mL of DMF. After all reagents were completely dissolved, 1.5 mL of hydrochloric acid was added to the solution as a mineralization agent. Subsequently, the solution was transferred into a polytetrafluoroethylene lined autoclave for solvothermal treatment at 120 °C for 24 h. After the autoclave naturally cooled down to room temperature, the dark-red powder was separated by filtration and washed with 100 mL of DMF, ethanol, and deionized water three times for remove unreacted ligands. Following this, it was dried in an oven at 60 °C for 24 h. The product was named UiO-66-NH<sub>2</sub>.

#### 2.2.2. Synthesis of UiO-66-CHO

The intermediate UiO-66-CHO was synthesized following a published method (Ji et al., 2021). After UiO-66-NH<sub>2</sub> was dried, 2.6g of UiO-66-NH<sub>2</sub> and 10 mL of glutaraldehyde were added to 50 mL of absolute ethanol. The mixture was stirred until UiO-66-NH<sub>2</sub> was thoroughly dispersed. Subsequently, the mixture was allowed to react for 24 h at a temperature of 80 °C. Upon completion of the reaction, the resultant dark yellow powder was filtered out. The collected product was then washed three times with 100 mL of ethanol and deionized water to removal unreacted glutaraldehyde, and dried in an oven at 60 °C for 24 h. The product was named UiO-66-CHO.

#### 2.2.3. Synthesis of mercapto-modified MOFs

3.3 g of UiO-66-CHO, 3.3 g of Na<sub>2</sub>CO<sub>3</sub>, 3.3 g of TCA or MTD and 10 mL of deionized water were added to 150 mL of DMF in a round bottom flask equipped with a magnetic stirrer. Once the mixture was fully dispersed, the reaction was conducted at 75 °C for 24 h. Subsequently, the solid was separated and washed with 100 mL of DMF three times to remove unreacted TCA or MTD, 100 mL of ethanol three times to eliminate DMF, and 200 mL of deionized water three times to remove Na<sub>2</sub>CO<sub>3</sub> along with residual organic solvents. The resulting dark yellow solid was dried in an oven at 60 °C for 24 h to remove residual ethanol and water. The products were named UiO-66-TCA and UiO-66-MTD, respectively. The whole synthesis route can be found in Scheme 1.



**Scheme 1.** Synthesis routes of UiO-66-TCA and UiO-66-MTD.

### 2.3. Characterization

FT-IR spectroscopy was conducted using an Affinity-1S spectrophotometer using KBr pellets over a wavenumber range of 400–4000 cm<sup>-1</sup> with a resolution of 1 cm<sup>-1</sup>. (Shimadzu, Japan). XRD patterns were obtained with a MiniFlex 600 with 2θ ranging from 5 to 80° collected at a scan rate of 5°/min using Cu Kα radiation ( $\lambda = 1.5406 \text{ \AA}$ ) (Rigaku, Japan). The morphology of the samples was examined using a field emission scanning electron microscope (FESEM) Sigma 500 (Zeiss, Germany). EDS and mapping images were analyzed with an XFlash 6130 with Zr, O, S and Pb (Zeiss, Germany). The specific surface area and pore structures of MOFs were determined using nitrogen adsorption data and the BET (Brunauer-Emmett-Teller) equation, performed on an ASAP 2460 at 298 K (Micromeritics, USA). Thermogravimetric analysis (TGA) was carried out using a Discovery SDT 650 Thermo-gravimeter with a heating rate of 10 °C min<sup>-1</sup> under nitrogen atmosphere (TA Instruments,

USA). XPS measurements were conducted with an ESCALAB 250Xi, the XPS spectra were fitted with a Shirley background and Gaussian-Lorentzian functions. (Thermo Scientific, USA). A thermal type constant temperature magnetic stirrer (DF-101S, China) controlled the reaction process and temperature. The concentrations of Pb(II), Hg(II), Cd (II), Mg(II) and Ba(II) were measured by inductively coupled plasma optical emission spectrometer(ICP-OES, Leeman Prodigy 7, USA). Zeta potential tests were performed using a Marvern Zetasizer Nano Series (Marvern Panalytical, Germany) at a voltage of 110–240 V and a frequency of 50/60 Hz from pH = 1 to 5 in deionized water.

### 2.4. Batch experiments

All adsorption experiments were performed in batch mode using 20 mL glass bottles containing 10 mL of metal ion solution and 10 mg of adsorbent. These were placed in a six-port temperature-controlled water

bath ( $\pm 0.1$  °C) to maintain constant temperature conditions. Adsorption isotherms were obtained by varying Pb(II) concentrations (400–1500 mg/L) at 30 °C, with equilibrium times determined from preliminary kinetic studies. Thermodynamic studies were conducted in a Pb(II) solution at temperatures varying from 20 °C to 70 °C. The pH of the solutions was adjusted to values between 1 and 5 using 1 M nitric acid and 1 M aqueous ammonia. Selectivity tests were conducted using 5 mg of adsorbent in 10 mL of metal ion solutions, each at 50 mg/L. The reusability of adsorbents was evaluated through five adsorption-desorption cycles, using 0.1M hydrochloric acid as the desorbing agent. All data represent the average of triplicate measurements.

### 2.5. DFT calculation

All density functional theory (DFT) calculations were performed by using the Dmol3 module in Materials Studio. The D3 correction approach (DFT-D3) was applied to account for van der Waals interactions. The exchange-functional was treated using the generalized gradient approximation (GGA) of Perdew-Burke-Ernzerhof (PBE) functional. The effective core potentials and double numerical plus polarization (DNP) basis were employed. Structural optimizations were performed minimizing the forces on each ion to below 0.002 Ha/Å. The energy and maximum displacement were set as  $1 \times 10^{-5}$  Ha/atom and 0.005 Å, respectively. The self-consistent calculations employed a convergence energy threshold of  $1 \times 10^{-6}$  Ha.

## 3. Results and discussion

### 3.1. Characterization of materials

#### 3.1.1. Structural and morphological characterizations

The XRD patterns of four MOFs are presented in Fig. 1a. The pattern of UiO-66-NH<sub>2</sub> displays prominent peaks at 7.42°, 8.56°, 12.14°, 17.22°, 22.29°, 25.69° and 30.72°, corresponding to the (111), (200), (222), (400), (511), (600) and (711) lattice planes of UiO-66-NH<sub>2</sub>, respectively. Consistent with the literature description, this indicates that UiO-66-NH<sub>2</sub> was successfully prepared (Gao et al., 2023). All modified MOFs exhibited diffraction patterns similar to the original MOF, suggesting that the crystal morphology was preserved during the modification process. In the XRD pattern of the modified MOFs, the appearance of a broad peak around 25° indicates amorphous surface-modified layer. The experimental XRD pattern of the MOFs closely matches the simulated pattern, confirming the successful preparation of the MOFs.

Prominent peaks corresponding to different functional groups (-NH<sub>2</sub>, C-N, Zr-O, etc.) are shown in Fig. 1b with the FT-IR spectra of various MOFs. For UiO-66-NH<sub>2</sub>, the -NH<sub>2</sub> group forms hydrogen bonds with water molecules, showing a broad peak located in 3465 to 3360 cm<sup>-1</sup>.

The peak at 1261 cm<sup>-1</sup> is attributed to C-N bond between benzene ring and amino group of ATA (Wu et al., 2018). The peaks at 576 cm<sup>-1</sup> and 667 cm<sup>-1</sup> correspond to the coordination bond of Zr-O and Zr-O<sub>2</sub>, respectively (Wang et al., 2022). The peaks at 1384, 1566 and 1658 cm<sup>-1</sup> are assigned to C-C, -COO<sup>-</sup> and C=N groups, respectively (Duan et al., 2023). For UiO-66-CHO, the peak at 1689 cm<sup>-1</sup> is attributed to C=O, while the peak at 2935 cm<sup>-1</sup> indicates the presence a glutaraldehyde carbon chain. For UiO-66-TCA and UiO-66-MTD, the peaks at 2461 and 2480 cm<sup>-1</sup> correspond to the mercapto group vibrations. The disappearance of the peak at 2935 cm<sup>-1</sup> suggests that the glutaraldehyde carbon chain is obscured by TCA and MTD.

The FESEM images of MOFs are depicted in Fig. 2. The images reveal that the modification process changed the surface topography of UiO-66-NH<sub>2</sub>. The original UiO-66-NH<sub>2</sub> consisted of irregular block-shaped aggregates with particle sizes roughly around 1 μm. However, the UiO-66-CHO showed that the block-shaped aggregates has disappeared. UiO-66-TCA and UiO-66-MTD show a rougher surface topography, which may be attributed to surface modification.

#### 3.1.2. N<sub>2</sub> adsorption-desorption determination

The N<sub>2</sub> adsorption-desorption isotherms reveal the pore characteristics of the MOFs (Fig. 3a–c), with specific surface areas and pore diameters of MOFs and additional pore parameters provided in Table S1 and Fig. S1, respectively. The isotherm for UiO-66-NH<sub>2</sub> shows a classic IUPAC Type I isotherm, typical of microporous materials, while those for UiO-66-TCA and UiO-66-MTD display Type III isotherms, with pronounced Type H2 hysteresis loops (Y. Zhang et al., 2023). This transformation originates from the conversion of some pores by modification groups into "ink-bottle" configurations during surface functionalization. These distinctive pores feature narrow necks and wide bodies, causing delayed desorption and pronounced hysteresis loops. However, most original pores of UiO-66-NH<sub>2</sub> become fully shielded after modification, the measured pore sizes actually reflect the pore dimensions of the surface modification layer, leading to apparent pore enlargement.

Notably, the BET surface areas of UiO-66-NH<sub>2</sub>, UiO-66-TCA and UiO-66-MTD are 1035.08 m<sup>2</sup>/g, 3.18 m<sup>2</sup>/g and 10.95 m<sup>2</sup>/g, respectively. Since the modification groups are much larger than the original amino side chains of UiO-66-NH<sub>2</sub>, and w their orientation toward the pore interior results in pore shielding, which is reflected in the decrease in the specific surface area on the BET surface area. The decrease in the BET surface area depends on the grafting rate and the size of the modified groups (Duan et al., 2023; Liu et al., 2019).

#### 3.1.3. TGA characterization

The thermal stability of MOFs was evaluated using a thermogravimetric analyzer. The TG curves of all MOFs are presented in Fig. 3d in the temperature range of 30–800 °C. The curves reveal three distinct

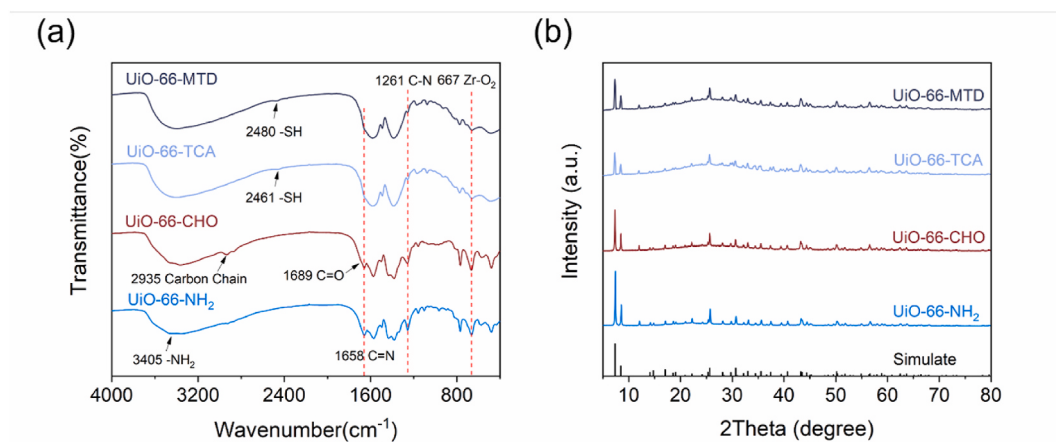


**Fig. 1.** (a) FT-IR spectra of UiO-66-NH<sub>2</sub>, UiO-66-CHO, UiO-66-TCA and UiO-66-MTD; (b) XRD patterns of UiO-66-NH<sub>2</sub>, UiO-66-CHO, UiO-66-TCA and UiO-66-MTD.

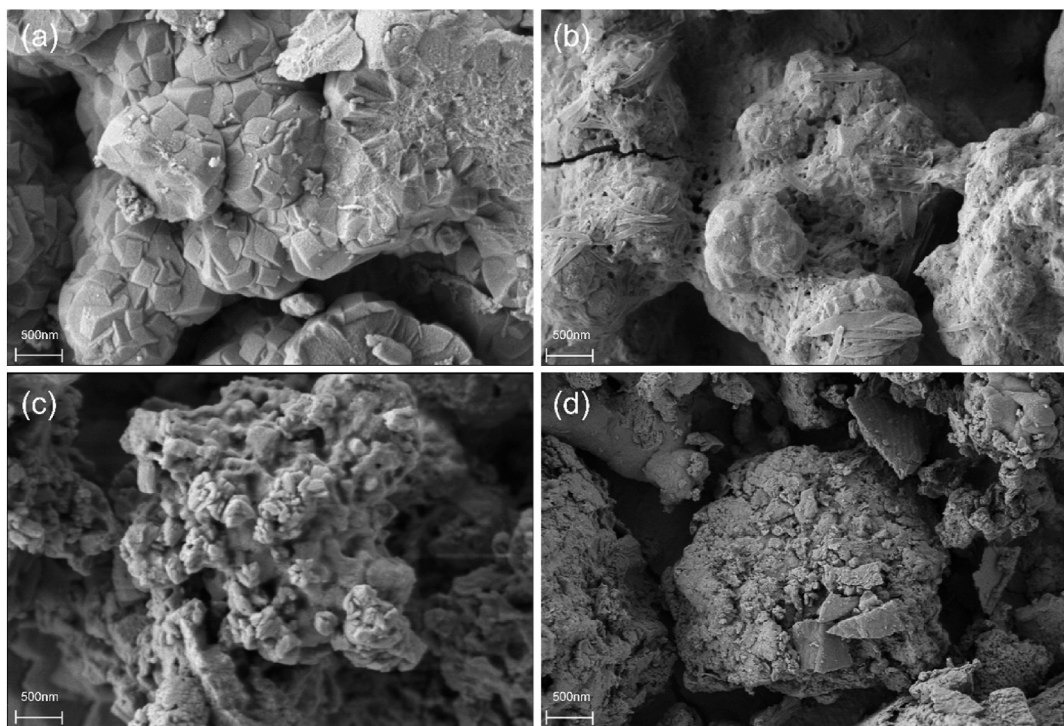


**Fig. 2.** SEM images of: (a) UiO-66- NH<sub>2</sub>; (b) UiO-66-CHO; (c) UiO-66-TCA; (d) UiO-66-MTD.

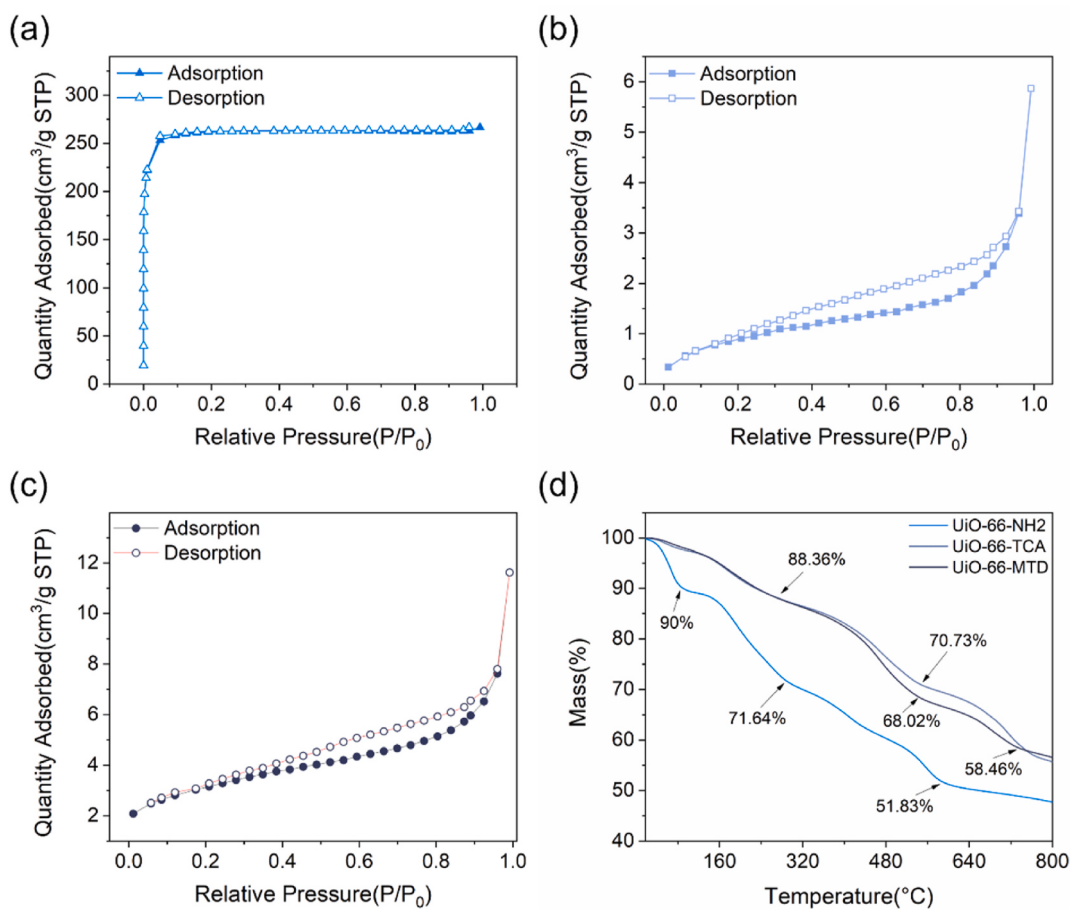


**Fig. 3.** (a-c) N<sub>2</sub> adsorption-desorption curves of UiO-66-NH<sub>2</sub> (a), UiO-66-TCA, (c)UiO-66-MTD; (d) TG curves of UiO-66-NH<sub>2</sub>, UiO-66-TCA and UiO-66-MTD.

stages of weight loss for the MOFs. The first stage, from 30 °C to 160 °C, exhibited approximately 5 % weight loss due to the loss of residual solvent. The second stage, spanning 160–600 °C with approximately 30 % weight loss, and was characterized by the decomposition and collapse of the organic frameworks, with the most rapid weight loss occurring in this range. The third stage, from 600 °C to 800 °C, represents the final phase of thermal decomposition, culminating in the transformation of the MOFs into zirconium dioxide (Sun et al., 2024).

Notably, the modified MOFs exhibit better thermal stability compared to UiO-66-NH<sub>2</sub>, while simultaneously demonstrating higher residual ash content. This is attributed to the surface of the modified MOF being loaded with a large number of triazine rings (UiO-66-TCA) and thiadiazole rings (UiO-66-MTD). According to the EDS analysis results (see section 3.3), the modified MOF surface contains a significant amount of sulfur. Both the triazine and thiadiazole rings possess flame-retardant properties, owing to their elevated thermal decomposition temperatures than those of common materials, thus enhancing the thermal stability of the modified MOFs. Additionally, because the modification layer of the MOF lacks oxygen atoms, sulfur and nitrogen are unable to form gaseous compounds during pyrolysis. Instead, these elements react with zirconium and carbon to form thermally stable solid residues, thereby increasing the ash contents (Suryapratha and Sethuraman, 2018; Yin et al., 2025).

### 3.2. Adsorption performance

#### 3.2.1. Adsorption kinetics

To further investigate the adsorption dynamics of UiO-66-TCA and UiO-66-MTD, kinetic experiments were conducted. The results are depicted in Fig. 4. Intraparticle diffusion model for UiO-66-TCA and

UiO-66-MTD are shown in Fig. S2. Fig. 4a illustrates the time-dependent adsorption behavior of UiO-66-TCA and UiO-66-MTD. Initially, in the first 20 min, the adsorption capacity of both materials increased rapidly, primarily due to surface diffusion. From 20 to 480 min, the rate of adsorption slowed down as intraparticle diffusion became the dominant mechanism, as indicated by the gradual slope of the curves. After 480 min, the curves plateaued, indicating the attainment of adsorption equilibrium. Fig. 4b to d presents the fit curves of three kinetic models, the pseudo-first-order model, the pseudo-second-order model, and the Elovich model. The equations for these models are provided in the Supplementary Materials, and the model parameters are listed in Text S1 and Table 1. Among the models, the pseudo-second-order model provided the best fit with R<sup>2</sup> values of 0.9992 and 0.9991 for UiO-66-TCA and UiO-66-MTD, respectively, indicating strong agreement with experimental data, suggesting that the adsorption of UiO-66-TCA and UiO-66-MTD is primarily chemisorptive, which refers to the adsorption process involving chemical bond formation between Pb(II) and adsorbent, typically characterized by high activation energies and irreversible

**Table 1**  
Kinetic parameters for adsorption of Pb(II) for UiO-66-TCA and UiO-66-MTD.

Kinetic models	UiO-66-TCA	UiO-66-MTD
Pseudo First Order	K <sub>1</sub> (min <sup>-1</sup> )	0.0080
	q <sub>e</sub> (mg/g)	154.39
	R <sup>2</sup>	0.8389
Pseudo Second Order	K <sub>2</sub> (g/mg·min <sup>-1</sup> )	4.0672
	q <sub>e</sub> (mg/g)	454.54
	R <sup>2</sup>	0.9992
Elovich	B(g/mg)	0.02737
	R <sup>2</sup>	0.9465
		0.9828

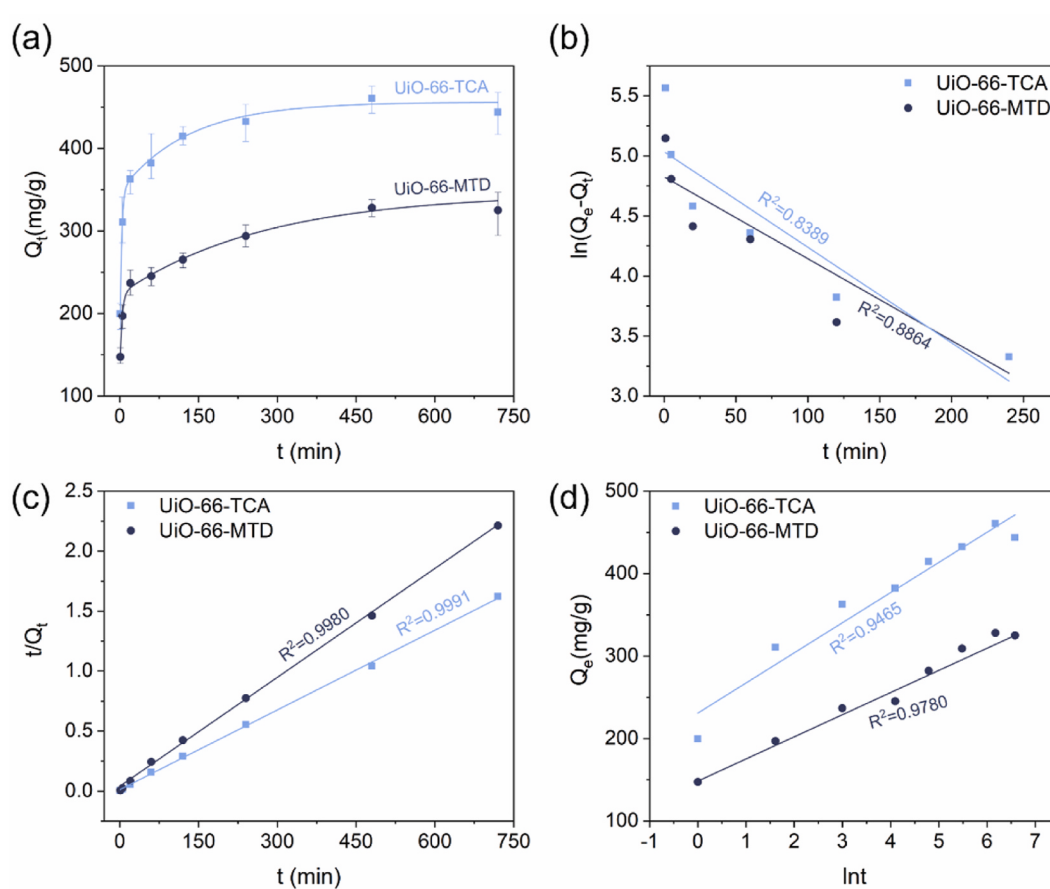


**Fig. 4.** (a) Kinetics curves of UiO-66-TCA and UiO-66-MTD; (b-d) fitting curves derived from the models based on (b) pseudo-first-order model, (c) pseudo-second-order, (d) Elovich model.

binding (Zhang et al., 2022).

### 3.2.2. Adsorption isotherm

The adsorption isotherms are illustrated in Fig. 5a, demonstrating a concentration-dependent adsorption behavior where UiO-66-TCA and UiO-66-MTD show increasing Pb(II) uptake with higher initial concentrations. This increase can be attributed to the equilibrium shifting rightward with rising concentrations. However, the adsorption rate decreases significantly beyond 600 mg/L due to the progressive saturation of available binding sites. To quantitatively characterize the adsorption mechanisms, the fitting curves for the Langmuir, Freundlich, and Temkin models are presented in Fig. 5b-d. The equations for these models are detailed in the Supplementary Materials. The relevant isothermal parameters and correlation coefficient ( $R^2$ ) of these models are shown in Table 2. By comparison, the  $R^2$  values of Langmuir models are larger than those of Freundlich and Temkin models, suggesting that the adsorption processes for UiO-66-TCA and UiO-66-MTD predominantly involve monolayer adsorption at independent binding sites.

Based on the adsorption parameters outlined in Table 2, UiO-66-TCA exhibits approximately twice the maximum adsorption capacity ( $Q_m$ ) of UiO-66-MTD. This significant difference is attributed to the use of one mercapto group in both TCA and MTD for substrate binding, with the unreacted mercapto groups remaining as two for TCA and one for MTD, respectively. The DFT calculation reveals that the interaction between the sulfur atom in the thiohemiacetal is significant. The C-S bond length in TCA increased from 1.8 Å to 4.5 Å upon Pb(II) adsorption, indicating significant structural distortion and strong Pb-S interactions. Additionally, the poor convergence observed during the geometry optimization

**Table 2**

Isotherm parameters using Langmuir, Freundlich, and Temkin models.

Isotherm models		UiO-66-TCA	UiO-66-MTD
Langmuir	$Q_m(\text{mg/g})$	967.66	464.91
	$K_L(\text{g/mg})$	0.0083	0.0155
	$R^2$	0.9982	0.9978
Freundlich	$K_F(\text{mg/g})(L/\text{mg})$	179.92	132.20
	$n$	4.0933	5.4230
	$R^2$	0.9831	0.9661
Temkin	$b_T(\text{kJ/mol})$	13.069	35.754
	$K_T(L/\text{g})$	0.9906	0.9982
	$R^2$	0.9969	0.9831

process indicates that adsorption at this site is improbable. Therefore, the available binding sites on UiO-66-TCA are approximately double those on UiO-66-MTD, which accounts for the observed disparity in  $Q_m$ .

For comparison, UiO-66-NH<sub>2</sub> was also evaluated, with its adsorption isotherm and corresponding fitting parameters presented in Fig. S3 and Table S2, respectively. The UiO-66-NH<sub>2</sub> exhibited adsorption behavior similar to UiO-66-TCA and UiO-66-MTD. The maximum adsorption capacity is determined by Langmuir model was found to be 115.10 mg/g. Specifically, UiO-66-TCA and UiO-66-MTD demonstrated 840.71 % and 403.92 % higher capacities relative to UiO-66-NH<sub>2</sub>, respectively. This indicates that surface modification has effectively enhanced the adsorption performance of UiO-66-NH<sub>2</sub>.

### 3.2.3. Adsorption thermodynamics

The temperature dependence of Pb(II) adsorption is demonstrated in Fig. 6a. As the temperature increased from 25 to 65 °C, the adsorption capacity rose from 440.66 mg/g to 513.54 mg/g, and from 282.89 mg/g

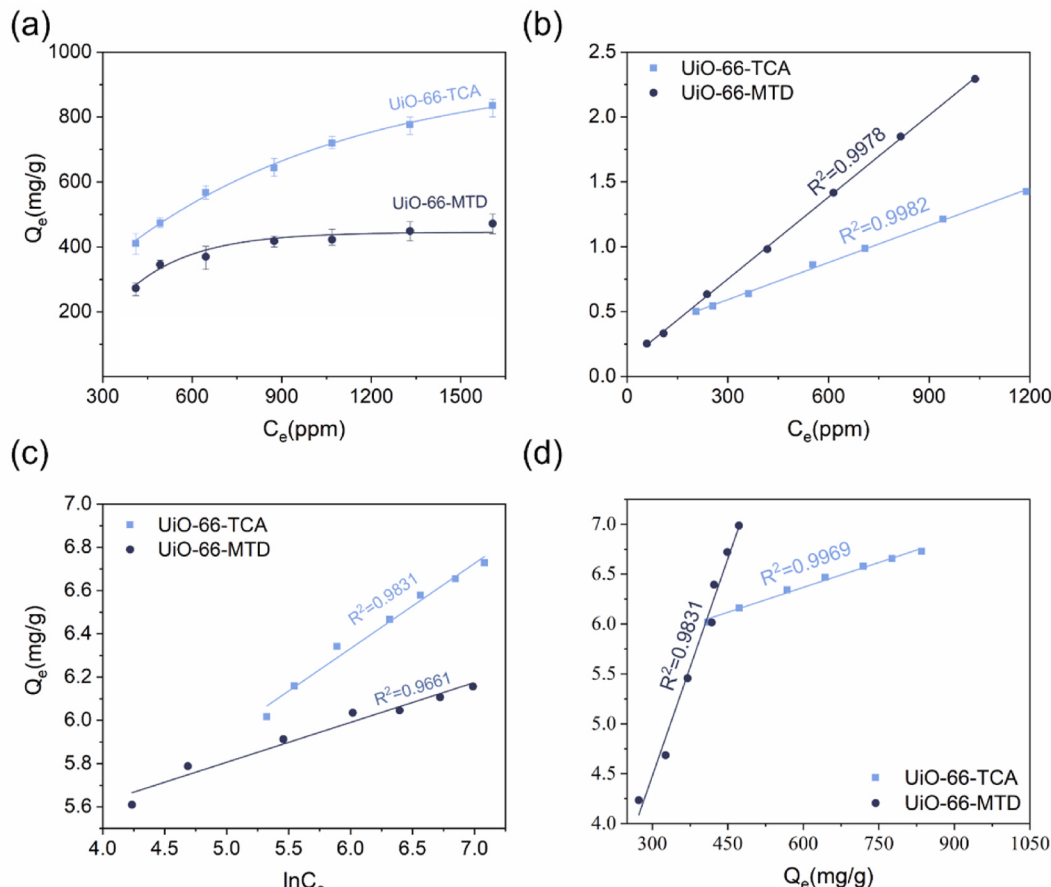


**Fig. 5.** (a) Adsorption isotherm curves of UiO-66-TCA and UiO-66-MTD; (b-d) fitting curves derived from the model based on (b) Langmuir model, (c) Freundlich model, (d) Temkin model.

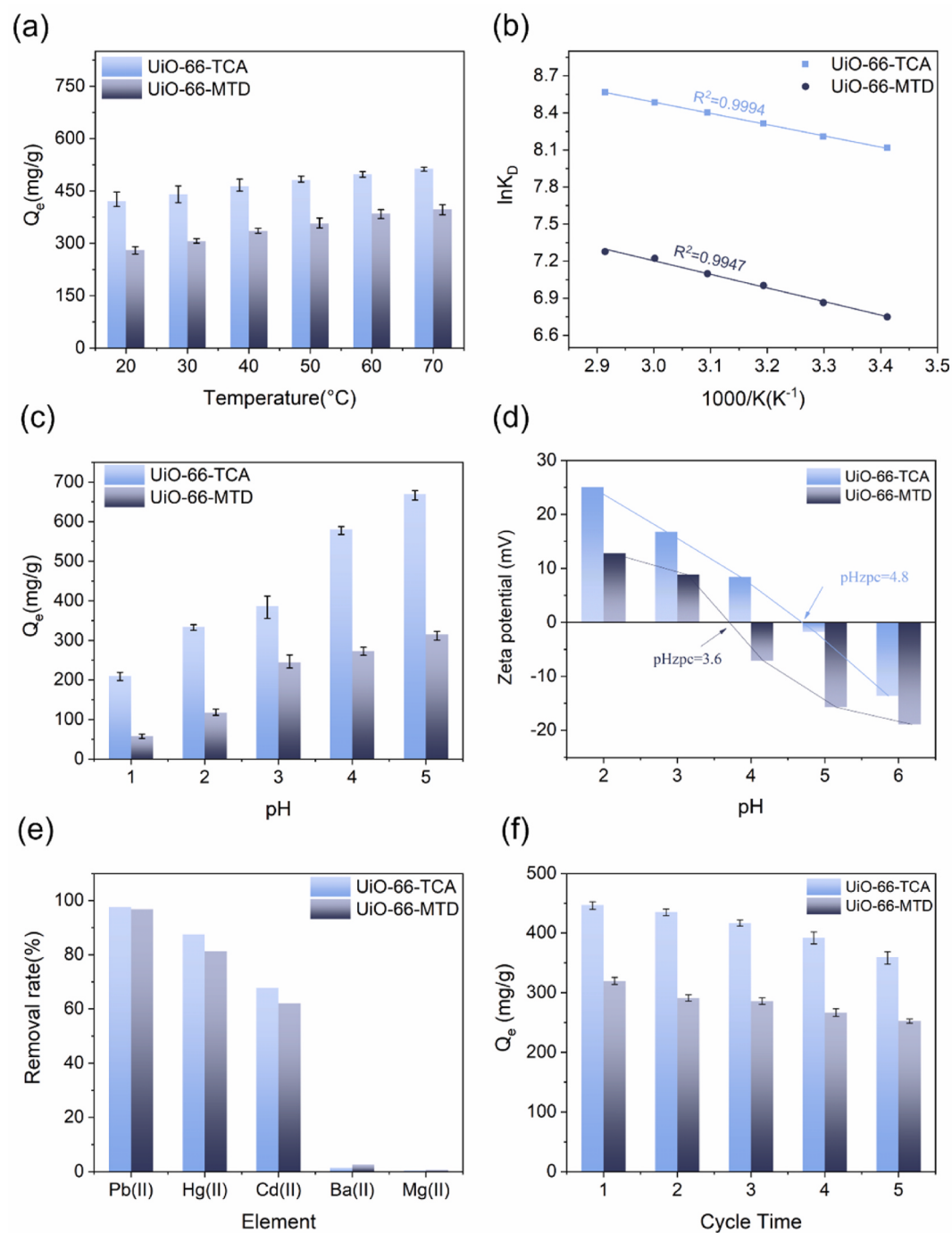


**Fig. 6.** (a) Effect of temperature; (b) fitting curves of van't Hoff equation; (c) effect of pH; (d) zeta potential testament of UiO-66-TCA and UiO-66-MTD; (e) different metal ions on adsorption; (f) reusability of regenerated adsorbents of Pb(II).

to 397.26 mg/g. To further elucidate the thermodynamics of the adsorption process, a linear relationship between  $\ln K_D$  and  $1000/T$  was derived using the van't Hoff equation. The resulting linear plot is depicted in Fig. 6b.

Thermodynamic parameters for UiO-66-TCA and UiO-66-MTD are presented in Table 3, calculation method is presented in Text S1. Based on these parameters, the negative Gibbs free energy change ( $\Delta G^\circ$ ) indicates that the adsorption process is spontaneous. The enthalpy change

**Table 3**  
Thermodynamic parameters for the adsorption of Pb(II) with MOFs.

Absorbent	$\Delta G^\circ$ (kJ/mol)						$\Delta H^\circ$ (kJ/mol)	$\Delta S^\circ$ (J/mol·K)
	20 °C	30 °C	40 °C	50 °C	60 °C	70 °C		
UiO-66-TCA	-17.98	-18.81	-19.68	-20.52	-21.34	-22.18	-6.24	-82.79
UiO-66-MTD	-16.45	-17.30	-18.23	-19.07	-20.01	-20.76	14.82	-85.26

( $\Delta H^\circ$ ) for UiO-66-TCA is negative, confirming that the adsorption process is exothermic. In contrast, the positive enthalpy change for UiO-66-MTD suggest that its adsorption process is endothermic. Additionally, an increase in temperature correlates with enhanced adsorption capacity. The observed decrease in entropy on the material surface during adsorption suggests a strong affinity of both adsorbents for Pb(II) (Sun et al., 2024).

### 3.2.4. Effect of initial pH value and reusability

Given the potential hydrolysis of Pb(II) to form Pb(OH)<sub>2</sub> precipitates at pH > 5.5, the pH effect on adsorption was systematically investigated over a pH range of 1–5. The adsorption results were shown in Fig. 6c. UiO-66-TCA and UiO-66-MTD both exhibited pH-dependent adsorption behavior, with capacity of UiO-66-TCA increasing from 210.25 mg/g at pH 1–670.04 mg/g at pH 5, and capacity of UiO-66-MTD increasing from 58.14 mg/g to 315.10 mg/g over a same pH range. It primarily driven by diminished electrostatic repulsion and enhanced coordination interactions. The zeta potential results were shown in Fig. 6d, the UiO-66-TCA showed decreasing potential from +25.1 mV (pH 2) to -13.6 mV (pH 6), with a pHzpc of 4.8, while UiO-66-MTD demonstrated more pronounced charge variation from +12.8 mV to -18.9 mV over the same range, with a lower pHzpc of 3.6. These measurements elucidate the adsorption mechanism - at pH < pHzpc, positively charged surfaces electrostatically repel Pb(II), limiting adsorption to coordination chemistry. As pH approaches and exceeds the pHzpc, the developing negative surface potential not only facilitates coordination between Pb (II) and mercapto groups but also introduces favorable electrostatic attraction with -S- sites (Zhang et al., 2024). Besides, the consistently lower zeta potential of UiO-66-MTD relative to UiO-66-TCA likely contributes to its more pronounced pH-dependent adsorption enhancement, as evidenced by comparative adsorption tests across the pH spectrum.

The reusability of an adsorbent is a critical factor in determining its viability for industrial applications. In this study, 0.1M HCl was used as the desorbent. Fig. 6f illustrates that after five adsorption cycles, the adsorption capacities of UiO-66-TCA and UiO-66-MTD were maintained at 76.08 % and 77.28 %, respectively.

The XRD patterns and FT-IR spectra of UiO-66-TCA and UiO-66-MTD after each cycle are shown in Fig. S5. The XRD patterns indicate that the crystalline structure was maintained after five cycles, although the peak became weaker in each cycle, suggesting that the crystallinity gradually decreases during the cycles.

Because the mercapto group in FT-IR spectrum are extremely weak, they are not a good characterization group for observing degradation processes. In addition, the thioacetal performs better than the imine group under weak acidic conditions, the degradation of UiO-66-TCA and UiO-66-MTD occurs mainly in the imine groups. The FT-IR spectrum reveals a progressive weakening of C=N bond signals during cycling experiments, confirming that the degradation of the modification layer is responsible for the reduced adsorption capacity (Mohammadi et al., 2024; Molavi and Salimi, 2025).

The mass retention rate and recovery rate data throughout the cycling experiments are summarized in Table S3. The recovery rates after each cycle was approximately 90 %. Furthermore, the recovery rate exhibited a gradual decline with increasing cycle numbers. The discrepancy between the recovered mass and the initial mass in adjacent cycles is due to the need for sampling in each cycle for XRD and FT-IR characterization. These results collectively demonstrate that the synthesized MOFs maintain effective regeneration capability, highlighting their potential value in the treatment of lead-contaminated industrial wastewater.

### 3.2.5. Adsorption Selectively

To evaluate the selective adsorption capacity of UiO-66-TCA and UiO-66-MTD, mixed ionic solutions were prepared by dissolving Pb (NO<sub>3</sub>)<sub>2</sub>, Cd(NO<sub>3</sub>)<sub>2</sub>, Ba(NO<sub>3</sub>)<sub>2</sub>, Hg(NO<sub>3</sub>)<sub>2</sub>, and Mg(NO<sub>3</sub>)<sub>2</sub>, each with a concentration of 50 mg/L. The removal rate is shown in Fig. 6e. As a

result, the Pb(II) removal rates reached 97.61 % and 96.82 %. In contrast, the removal rates for Cd(II) and Hg(II) were only 67.78 % and 87.57 % for UiO-66-TCA, and 62.02 % and 81.38 % for UiO-66-MTD, respectively. Negligible adsorption occurred for Ba(II) and Mg(II). As illustrated in Fig. S3, UiO-66-TCA and UiO-66-MTD exhibit superior selectivity for Pb(II) compared to other metal ions. Specifically, the selectivity coefficients for Pb(II)/Hg(II) for UiO-66-TCA and UiO-66-MTD are 5.80 and 7.00, respectively. In contrast, the selectivity coefficients for Pb(II)/Cd(II) are 19.41 and 18.64. Notably, for Pb(II)/Mg (II) and Pb(II)/Ba(II), the selectivity coefficients increase significantly to 2700.17 and 1182.56, and 7967.20 and 4653.64, respectively.

According to the HSAB theory, soft acids (e.g., Pb(II), Hg(II)) preferentially interact with soft bases (e.g., -SH) due to their high polarizability and covalent bonding tendencies, while hard acids (e.g., Mg(II), Ba(II)) interact weakly with soft bases. Due to the different degrees of "softness" for the five metal ions, UiO-66-TCA and UiO-66-MTD exhibit different adsorption capacities for each metal ion. Mercapto groups show a stronger affinity and thus better adsorption performance for "softer" metals such as Pb, Hg, and Cd. In contrast, they exhibit weaker adsorption for relatively hard acids such as Mg and Ba (Cao et al., 2020).

### 3.3. Adsorption mechanism

To elucidate the interaction between the adsorbent and Pb(II) during the adsorption process, various characterization techniques, including SEM mapping of elemental distribution, EDS, and XPS, were employed to analyze the UiO-66-TCA sample. The EDS spectra, illustrated in Fig. 7f, demonstrate that the surface weight percentage of the Pb element is 33.80 %. This indicates that the surface of UiO-66-TCA was coated with a Pb layer due to sorption following the adsorption process. Figs. 7 and 8d display the mapping results, indicating that Zr, S, and O are predominant on the surface of UiO-66-TCA, confirming that the modified UiO-66-NH<sub>2</sub> surface is enriched with mercapto groups. Fig. 7e confirms the uniform distribution of elemental Pb on the surface of UiO-66-TCA post-adsorption, further demonstrating the effective adsorption of Pb(II).

The XPS survey spectra of UiO-66-TCA are shown in Fig. 8a to d. Fig. 8a shows the XPS spectra, where it can be observed that there is no Pb peak in the spectra before adsorption, whereas a Pb peak is present in the spectra after adsorption. This indicates that Pb was successfully loaded onto the surface of UiO-66-TCA after adsorption. Fig. 8b and c provide the XPS spectra of S2p before and after adsorption. The binding energy of S2p can be divided into two distinct peaks, corresponding to S2p<sub>3/2</sub> and S2p<sub>1/2</sub>, respectively. In the spectra before adsorption, S2p<sub>3/2</sub> and S2p<sub>1/2</sub> are positioned at 161.95 eV and 168.32 eV, respectively. These values shift to 162.40 eV and 167.85 eV after adsorption, respectively. Furthermore, there are observable changes in peak area, with the S2p<sub>1/2</sub> peak demonstrating a significant enhancement compared to its pre-adsorption state, confirming that there is a strong chelation between Pb(II) and the -SH groups on UiO-66-TCA (X. Liu, L. K. Fu et al., 2023; Tang et al., 2021). The spectra of Pb4f, as shown in Fig. 8d, can be divided into two peaks located at 138.79 eV and 143.64 eV, corresponding to Pb4f<sub>7/2</sub> and Pb4f<sub>5/2</sub>, respectively (Ruan et al., 2022; Xiang et al., 2024). Notably, UiO-66-TCA prior to adsorption did not display a distinct peak at these same locations.

To mechanically understand how surface modification groups in UiO-66-NH<sub>2</sub> on the adsorption of Pb(II), density functional theory (DFT) calculations were carried out to investigate the interaction between Pb (II) and the two active sites. The geometric optimizations for the modified MOFs and Pb systems were performed. The DFT calculation results and electrostatic potential distribution are presented in Figs. S6 and S7. The presence of mercapto groups facilitates strong coordination interactions between Pb(II) and the modified sites, leading to the formation of stable Pb-S bonds. Calculated Pb-S bond lengths of 2.81 Å (UiO-66-TCA) and 3.32 Å (UiO-66-MTD), respectively. The DFT calculations reveal adsorption energies of -0.3657 eV and -0.3623 eV for Pb

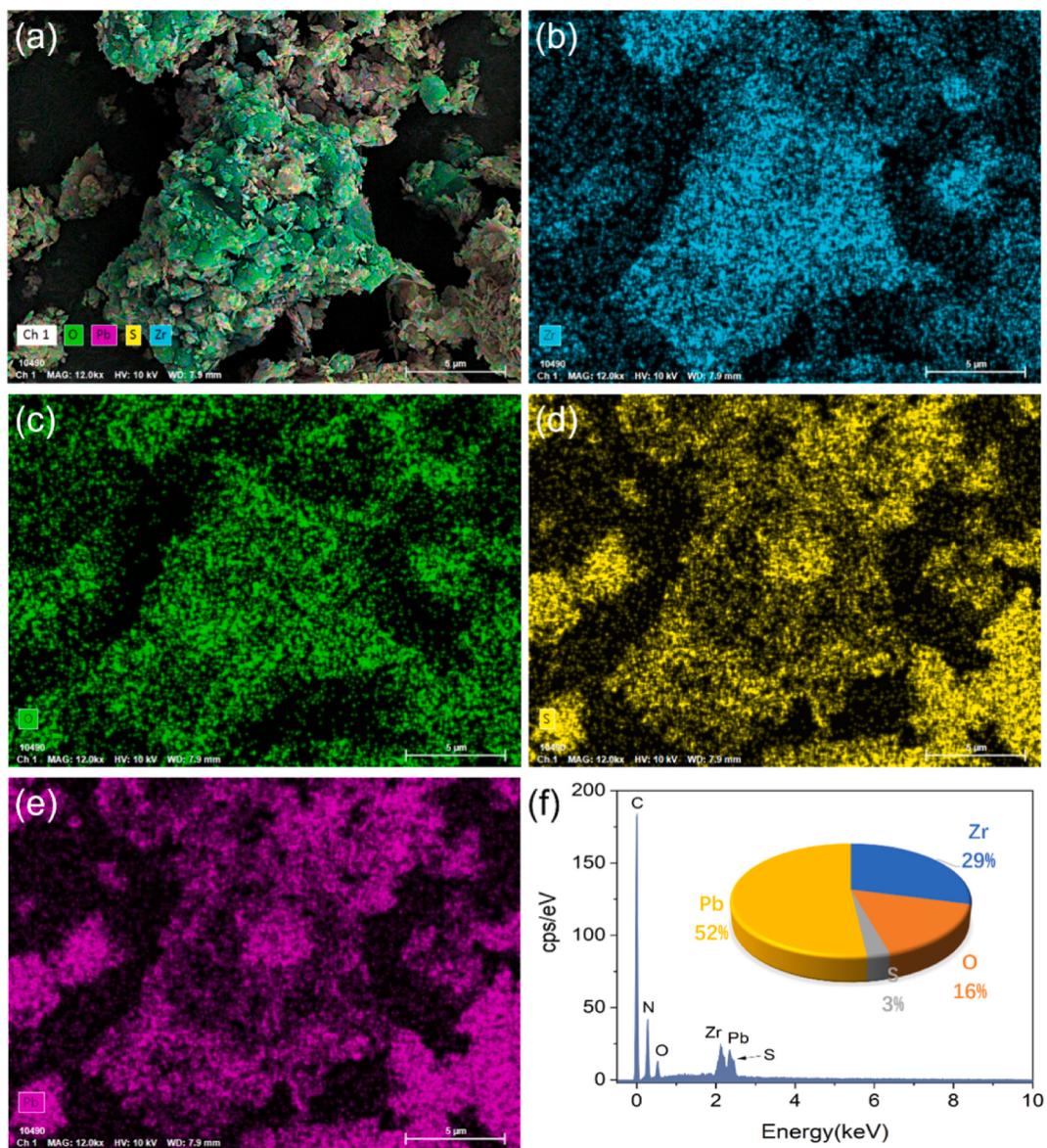


**Fig. 7.** (a–e) SEM mapping images of UiO-66-TCA after adsorption: (a) total, (b) Zr, (c) O, (d) S, (e) Pb; (f) EDS spectrum of UiO-66-TCA after adsorption.

(II) with each mercapto groups in UiO-66-TCA, respectively, and  $-0.3420$  eV for UiO-66-MTD, suggesting that the adsorption process is spontaneous.

Notably, a more negative binding energy generally indicates a stronger interaction between the metal-adsorbent complexes. The computational models are depicted in Fig. S8, DFT calculation results of the adsorption energies for five ions are presented in Fig. 9. The coordination cluster of UiO-66 has been removed to simplify the calculation. Among these, Pb ions exhibit the lowest adsorption energy, followed by Hg and Cd ions, suggesting that the affinities toward these three ions are ranked as Pb > Hg > Cd. Moreover, the calculations indicate that Mg and Ba ions exhibit positive adsorption energies in both UiO-66-TCA and UiO-66-MTD, suggesting that the adsorption processes are unlikely to occur spontaneously. This observation helps explain the very low adsorption capacities of Mg and Ba ions on the UiO-66-TCA and UiO-66-MTD.

Highest occupied molecular orbital (HOMO) and lowest unoccupied molecular orbital (LUMO), through intramolecular charge transfer, provide critical insights into quantum chemistry. Fig. S8 illustrates the HOMO and LUMO of UiO-66-TCA and UiO-66-MTD before and after adsorption. Table S3 shows the eigenvalue of HOMO and LUMO and

energy gaps ( $\Delta E$ ) for MOFs before and after adsorption.

According to Fig. S9, the frontier molecular orbital analysis reveals distinct electronic distributions before and after Pb(II) adsorption. Prior to adsorption, the HOMO of UiO-66-TCA is primarily localized on the organic ligands, whereas the LUMO are situated on the zirconium coordination clusters. In contrast, UiO-66-MTD exhibits an reversed orbital localization, with HOMO concentrated on the coordination clusters and LUMO on the modified thiadiazole groups. Following Pb(II) adsorption, both HOMO and LUMO of UiO-66-TCA were shift to the lead ions coordinated with thiol groups, indicating strong orbital hybridization. In contrast, UiO-66-MTD maintains its HOMO position on the coordination clusters while only the LUMO shifts to Pb(II)-thiol complexes, suggesting a different charge transfer mechanism. Energy gap calculations reveal significant changes after adsorption. The energy gaps decrease from 2.2496 eV to 0.09943 eV for UiO-66-TCA and from 2.2490 eV to 0.6403 eV for UiO-66-MTD. This substantial reductions in energy gaps suggest that the molecules are excited after adsorption, and Pb(II) ions have been successfully adsorbed onto the MOF surface. Moreover, the greater reduction in the energy gap of UiO-66-TCA compared to UiO-66-MTD after adsorption further explains why UiO-66-TCA exhibits stronger adsorption capabilities than UiO-66-MTD.

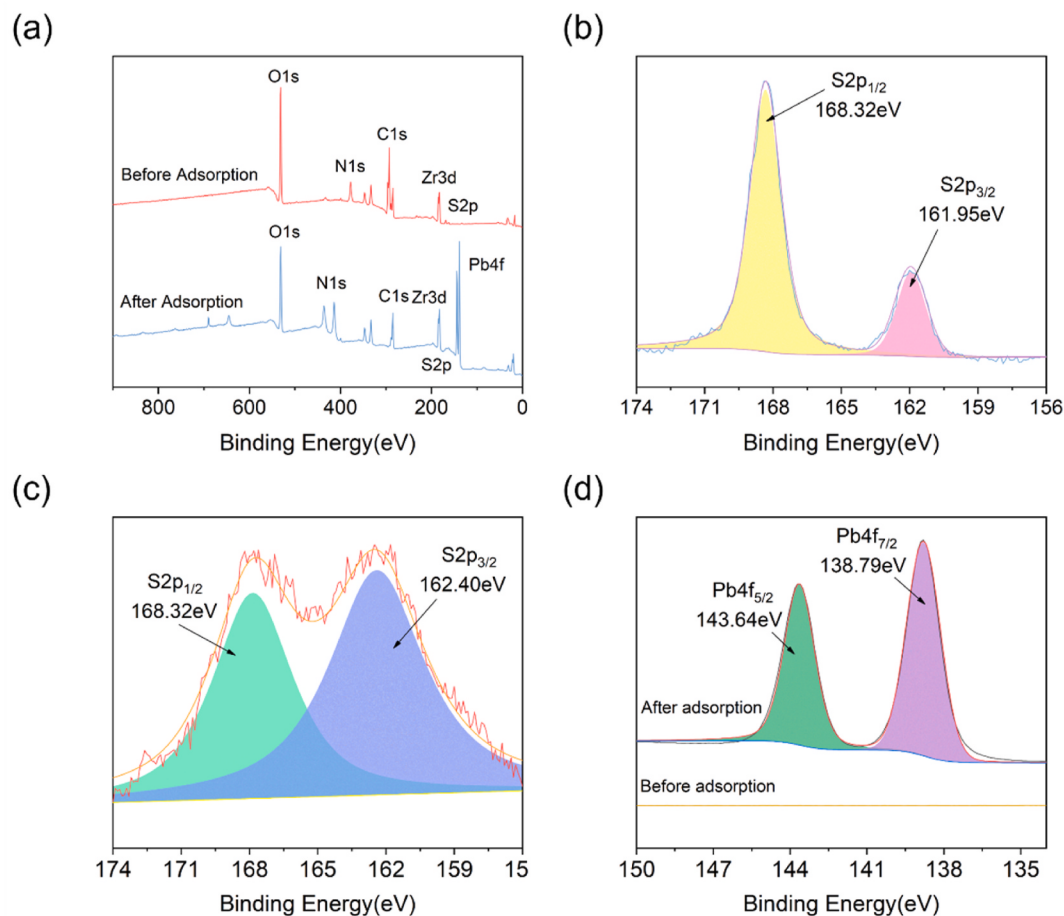


**Fig. 8.** XPS spectra of (a) survey, (b) Pb4f, (c) S2p before adsorption and (d) S2p after adsorption.

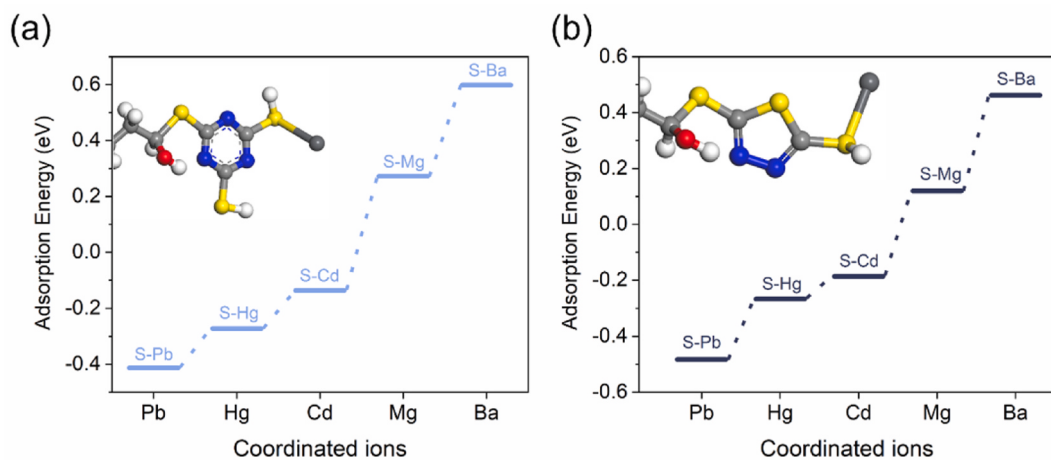


**Fig. 9.** Calculated adsorption energy diagram of (a) UiO-66-TCA, (b) UiO-66-MTD.

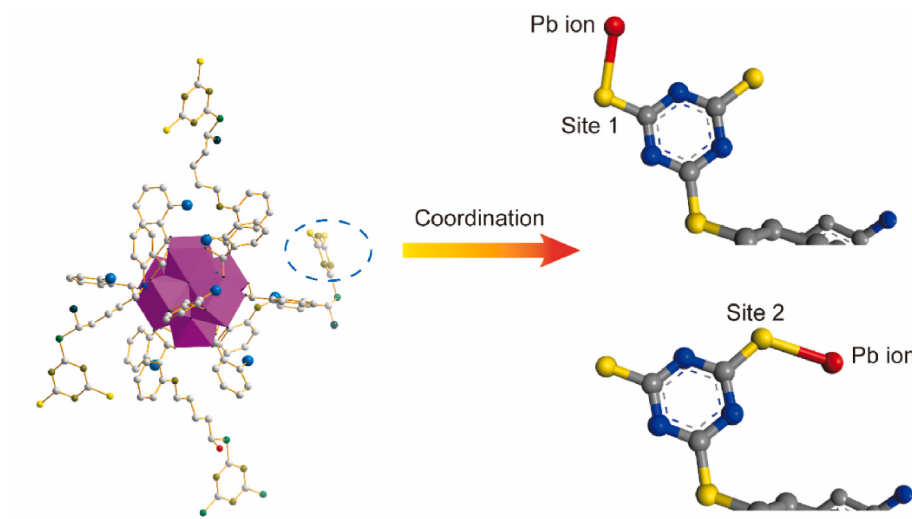
(Allal et al., 2020; García et al., 2015; Zhang et al., 2021).

According to the above analysis, the parameters including zeta potential, adsorption site and adsorption energy synergistically affect the adsorption properties of UiO-66-TCA and UiO-66-MTD. As shown in Scheme 2, the modified MOF surfaces provide abundant sulfur coordination sites, which is beneficial for the boosted adsorption performance towards Pb(II) from aqueous solution. XPS analysis confirmed the formation of Pb-S bonds, with S2p<sub>3/2</sub> binding energy shifts of +0.45 eV and new strong Pb(II) peaks were detected in the after-adsorption sample

consistent with Pb-S coordination interaction. DFT calculations confirmed that the Pb-S coordination bonds are the dominant adsorption mechanism. The dominant adsorption mechanism involves Pb-S coordinate bond formation between Pb(II) and mercapto group.

#### 3.4. Comparison of performance with previous works

Comparing the thiol-modified MOFs with previously reported adsorbents for Pb(II) is crucial. Table 4 summarizes comparative



**Scheme 2.** Possible adsorption mechanism of mercapto modified UiO-66 for Pb(II).

**Table 4**  
Comparison of previous adsorbents for removal of Pb(II).

Adsorbent	Maximum capacity (mg/g)	Reference
PNPD/KH550-BT	867.1	Li et al. (2024)
APTES/BC/MXene	323.17	Ijaz et al. (2024)
PT-COFs	940	Alneyadi (2025)
COF-NHOH	368.68	Xiang et al. (2024)
UiO-DCCA	353.29	(Liu et al., 2023)
Mg@MIL-101(Fe)/NH <sub>2</sub> -MIL-125(Ti) bis-MIL composites	320.914	Guo et al. (2024)
Defective SO <sub>3</sub> H-MIL-101(Cr)	189.6	Ren et al. (2023)
UiO-66-TCA	967.66	This work
UiO-66-MTD	464.91	This work

adsorption capacities of Pb(II) by several different adsorbents, including polymers, MXenes, covalent organic frameworks (COFs), and various MOFs. Notably, the adsorption capacities of UiO-66-TCA and UiO-66-MTD exceed most listed adsorbents, thereby confirming their superior performance.

#### 4. Conclusion

This study developed two novel thiol-modified MOFs based on UiO-66-NH<sub>2</sub>, achieving precise anchoring of sulfur-active sites through a directional modification strategy to enable efficient Pb(II) adsorption. Structural characterization confirmed the successful chemical grafting of modified groups onto the substrate while maintaining the original crystal structure throughout the modification process. Adsorption experiments revealed that the modified MOFs followed pseudo-second-order kinetics and the Langmuir adsorption model. Under optimized conditions (pH 4.5, 35 °C), the Langmuir-modeled maximum adsorption capacities reached 967.66 mg/g for UiO-66-TCA and 464.91 mg/g for UiO-66-MTD, with both materials demonstrating superior Pb(II) selectivity. Zeta potential measurements indicated partial influence of surface charge on adsorption behavior, while XPS analysis and DFT calculations identified sulfur atoms in the modified groups as the dominant adsorption sites. This thiol-engineering strategy enables novel approach for deep purification of lead-contaminated industrial wastewater, particularly in complex aqueous environments. Future studies

could extend this modification strategy to other heavy metal systems, validate scalability through pilot-scale testing with real effluents, and investigate sulfur coordination microenvironment engineering to enhance selectivity.

#### CRediT authorship contribution statement

**Lejie Zhu:** Resources, Investigation, Conceptualization. **Qiong Ouyang:** Writing – review & editing. **Donghao Liu:** Writing – original draft, Methodology, Formal analysis. **Jian Zhu:** Supervision. **Yu Zhang:** Supervision. **Jiaqiuqi Zhang:** Writing – review & editing, Supervision. **Kaiyin Shao:** Validation, Investigation. **Chengshuai Liu:** Writing – review & editing, Supervision, Project administration.

#### Declaration of competing interest

The authors declare that they have no known competing financial interests or personal relationships that could have appeared to influence the work reported in this paper.

#### Appendix A. Supplementary data

Supplementary data to this article can be found online at <https://doi.org/10.1016/j.jenvman.2025.126642>.

#### Data availability

No data was used for the research described in the article.

#### References

- Abdollahi, N., Akbar Razavi, S.A., Morsali, A., Hu, M.-L., 2020. High capacity Hg(II) and Pb(II) removal using MOF-based nanocomposite: cooperative effects of pore functionalization and surface-charge modulation. *J. Hazard Mater.* 387, 121667. <https://doi.org/10.1016/j.jhazmat.2019.121667>.
- Ahmadijokani, F., Molavi, H., Rezakazemi, M., Tajahmad, S., Bahi, A., Ko, F., Aminabhavi, T.M., Li, J.-R., Arjmand, M., 2022. UiO-66 metal–organic frameworks in water treatment: a critical review. *Prog. Mater. Sci.* 125, 100904. <https://doi.org/10.1016/j.pmatsci.2021.100904>.
- Akinterinwa, A., Reuben, U., Atiku, J.U., Adamu, M., 2022. Focus on the removal of lead and cadmium ions from aqueous solutions using starch derivatives: a review. *Carbohydr. Polym.* 290, 119463. <https://doi.org/10.1016/j.carbpol.2022.119463>.
- Al-Akeel, K.A., Al-Fredan, M.A., Desoky, E.S.M., 2021. Impact of wastewater discharge on the plant diversity, community structure and heavy metal pollution of range plants in eastern Saudi Arabia. *Saudi J. Biol. Sci.* 28 (12), 7367–7372. <https://doi.org/10.1016/j.sjbs.2021.08.059>.
- Al-Janabi, M.B., Mohammed, M.A., Aloabaidy, A.A., Al-Furaiji, M.H., 2023. Use of low-cost adsorbent for copper and lead removal from aqueous solutions. *Journal of*

- Ecological Engineering 24 (9), 19–26. <https://doi.org/10.12911/22998993/167950>.
- Albrektiene-Placake, R., Baziene, K., Gargasas, J., 2023. Investigation on applying biodegradable material for removal of various substances (Fluorides, Nitrates and lead) from water. Materials 16 (19), 6519. <https://doi.org/10.3390/ma16196519>.
- Alivand, M.S., Tehrani, N.H.M.H., Askarieh, M., Ghasemy, E., Esrafilii, M.D., Ahmadi, R., Anisi, H., Tavakoli, O., Rashidi, A., 2021. Defect engineering-induced porosity in graphene quantum dots embedded metal-organic frameworks for enhanced benzene and toluene adsorption. *J. Hazard Mater.* 416, 125973. <https://doi.org/10.1016/j.jhazmat.2021.125973>.
- Allal, H., Belhocine, Y., Rahali, S., Damous, M., Ammouchi, N., 2020. Structural, electronic, and energetic investigations of acrolein adsorption on B36 borophene nanosheet: a dispersion-corrected DFT insight. *J. Mol. Model.* 26 (6), 128. <https://doi.org/10.1007/s00894-020-04388-3>.
- Aleyadi, S.S., 2025. Phosphazene-based covalent organic framework: advanced lead-capture material with visual indicator for efficient water purification. *Journal of Hazardous Materials Advances* 17, 12. <https://doi.org/10.1016/j.hazadv.2025.100593>.
- Baghayeri, M., Alinezhad, H., Fayazi, M., Tarahomi, M., Ghanei-Motlagh, R., Maleki, B., 2019. A novel electrochemical sensor based on a glassy carbon electrode modified with dendrimer functionalized magnetic graphene oxide for simultaneous determination of trace Pb(II) and Cd(II). *Electrochim. Acta* 312, 80–88. <https://doi.org/10.1016/j.electacta.2019.04.180>.
- Baghayeri, M., Amiri, A., Maleki, B., Alizadeh, Z., Reiser, O., 2018. A simple approach for simultaneous detection of cadmium(II) and lead(II) based on glutathione coated magnetic nanoparticles as a highly selective electrochemical probe. *Sensor. Actuator. B Chem.* 273, 1442–1450. <https://doi.org/10.1016/j.snb.2018.07.063>.
- Bai, T., Zhao, J.X., Tian, L.X., Zhang, L.M., Jin, Z.P., 2024. The adsorption of Pb(II) from aqueous solution using KOH-modified Banana Peel hydrothermal carbon: adsorption properties and mechanistic studies. *Materials* 17 (2), 311. <https://doi.org/10.3390/ma17020311>.
- Cao, Y., Hu, X., Zhu, C., Zhou, S., Li, R., Shi, H., Miao, S., Vakili, M., Wang, W., Qi, D., 2020. Sulphydryl functionalized covalent organic framework as an efficient adsorbent for selective Pb (II) removal. *Colloids Surf. A Physicochem. Eng. Asp.* 600, 125004. <https://doi.org/10.1016/j.colsurfa.2020.125004>.
- Chen, J., Liao, C., Guo, X.X., Hou, S.C., He, W.D., 2022. PAAO cryogels from amidoximated P(acrylic acid-co-acrylonitrile) for the adsorption of lead ion. *Eur. Polym. J.* 171, 12. <https://doi.org/10.1016/j.eurpolymj.2022.111192>.
- Chowdhury, I.R., Chowdhury, S., Mazumder, M.A., Al-Ahmed, A., 2022. Removal of lead ions ( $Pb^{2+}$ ) from water and wastewater: a review on the low-cost adsorbents. *Appl. Water Sci.* 12 (8), 185. <https://doi.org/10.1007/s13201-022-01703-6>.
- Cui, W.L., Tang, K., Chen, Y.Q., Chen, Z., Lan, Y.H., Hong, Y.B., Lan, W.G., 2024. Regulating the particle sizes of NaA molecular sieves toward enhanced heavy metal ion adsorption. *New J. Chem.* 48 (17), 7863–7874. <https://doi.org/10.1039/d3nj05924c>.
- Duan, X., Wang, K., Wang, L., Cao, L., Sui, J., Lin, H., 2023. A novel UIO-66-NH<sub>2</sub>@TA adsorbent for effective solid-phase extraction of Pb (II) from environmental water and juices. *Colloids Surf. A Physicochem. Eng. Asp.* 671, 131700. <https://doi.org/10.1016/j.colsurfa.2023.131700>.
- Gao, Y., Yao, L., Zhang, S., Yue, Q., Yin, W., 2023. Versatile crosslinking synthesis of an EDTA-modified UIO-66-NH<sub>2</sub>/cotton fabric composite for simultaneous capture of heavy metals and dyes and efficient degradation of organophosphate. *Environ. Pollut.* 316, 120622. <https://doi.org/10.1016/j.envpol.2022.120622>.
- Garcia, G., Atilhan, M., Aparicio, S., 2015. Adsorption of choline benzoate ionic liquid on grapheme, silicene, germanene and boron-nitride nanosheets: a DFT perspective. *Phys. Chem. Chem. Phys.* 17 (25), 16315–16326. <https://doi.org/10.1039/c5cp02432c>.
- Gatabi, J., Sarrafi, Y., Lakouraj, M.M., Taghavi, M., 2020. Facile and efficient removal of Pb(II) from aqueous solution by chitosan-lead ion imprinted polymer network. *Chemosphere* 240, 124772. <https://doi.org/10.1016/j.chemosphere.2019.124772>.
- Guo, Z., Wu, X., Meng, J., Li, X., Li, Y., Hu, L., 2024. Preparation of Mg@MIL-101(Fe)/NH<sub>2</sub>-MIL-125(Ti) bis-MIL composites and their sorption performance towards Pb(II) from aqueous solution. *Sep. Purif. Technol.* 339, 126692. <https://doi.org/10.1016/j.seppur.2024.126692>.
- He, C., Wang, J., Qu, L., Zhang, X., 2024. Rational construction of MoS<sub>x</sub> via defect engineering for efficient removal of mercury ions from aqueous solution. *J. Clean. Prod.* 435, 140507. <https://doi.org/10.1016/j.jclepro.2023.140507>.
- He, J., Xiong, D., Zhou, P., Xiao, X., Ni, F., Deng, S., Shen, F., Tian, D., Long, L., Luo, L., 2020. A novel homogenous in-situ generated ferrilhydrite nanoparticles/polyethersulfone composite membrane for removal of lead from water: development, characterization, performance and mechanism. *Chem. Eng. J.* 393, 124696. <https://doi.org/10.1016/j.cej.2020.124696>.
- Ijaz, I., Bukhari, A., Nazir, A., Gilani, E., Zain, H., Hussain, S., Attia, s., Ifseisi, A.A., Ahmad, H., 2024. Enhanced selective adsorption capacity of lead (II) from complex wastewater by aminopropyltriethoxysilane-functionalized biochar grafted on the MXene based on anion-synergism. *Mater. Chem. Phys.* 314, 128929. <https://doi.org/10.1016/j.matchemphys.2024.128929>.
- Ismail, U.M., Omaizi, S.A., Vohra, M.S., 2023. Aqueous Pb(II) removal using ZIF-60: adsorption studies, response surface methodology and machine learning predictions. *Nanomaterials* 13 (8), 1402. <https://doi.org/10.3390/nano13081402>.
- Ji, Z., Sun, H., Zhu, Y., Zhang, D., Wang, L., Dai, F., Zhao, Y., Chen, L., 2021. Enhanced selective removal of lead ions using a functionalized PAMAM@UiO-66-NH<sub>2</sub> nanocomposite: experiment and mechanism. *Microporous Mesoporous Mater.* 328, 111433. <https://doi.org/10.1016/j.micromeso.2021.111433>.
- Kypritudou, Z., El-Bassi, L., Jellali, S., Kinigopoulou, V., Tziritis, E., Akroud, H., Jeguirim, M., Doulgeris, C., 2022. Lead removal from aqueous solutions by olive mill wastes derived biochar: batch experiments and geochemical modelling. *J. Environ. Manag.* 318, 115562. <https://doi.org/10.1016/j.jenvman.2022.115562>.
- Lach, J., Okoniewska, E., 2024. Equilibrium, kinetic, and diffusion mechanism of lead(II) and cadmium(II) adsorption onto commercial activated carbons. *Molecules* 29 (11), 23. <https://doi.org/10.3390/molecules29112418>.
- Li, X., Zhang, K.J., Xue, Y.W., 2022. Continuous immobilization of lead by biominerilization in a fluidized-bed biofilm reactor. *J. Clean. Prod.* 379, 134765. <https://doi.org/10.1016/j.jclepro.2022.134765>.
- Li, X.H., Xu, Z.H., Meng, Q., Chen, Y., Xu, L.S., Zhang, G.L., 2024. Synthesis of Schiff base polymer/black talc nanocomposites based on m-phenylenediamine with enhanced separation performance for lead adsorption. *Sep. Purif. Technol.* 341, 11. <https://doi.org/10.1016/j.seppur.2024.126874>.
- Liu, F., Xiong, W., Feng, X., Cheng, G., Shi, L., Chen, D., Zhang, Y., 2019. Highly recyclable cysteamine-modified acid-resistant MOFs for enhancing Hg (II) removal from water. *Environ. Technol.* 41 (23), 3094–3104. <https://doi.org/10.1080/09593303.2019.1595804>.
- Liu, H., Baghayeri, M., Amiri, A., Karimabadi, F., Nodehi, M., Fayazi, M., Maleki, B., Zare, E.N., Kaffash, A., 2023. A strategy for As(III) determination based on ultrafine gold nanoparticles decorated on magnetic graphene oxide. *Environ. Res.* 231, 116177. <https://doi.org/10.1016/j.envres.2023.116177>.
- Liu, L.X., Wu, L.D., Chen, Y., Ma, Y.F., Lin, L., Li, S., Yang, X.J., Chen, H., Duan, G.J., 2024. Synthesis of stable mesoporous Zr-MOFs using pyrazine-containing ligand for efficient capture of Pb(II) in wastewater. *J. Environ. Chem. Eng.* 12 (3), 112543. <https://doi.org/10.1016/j.jece.2024.112543>.
- Liu, X., Fu, L.K., Liu, H.L., Zhang, D.K., Xiong, C., Wang, S.X., Zhang, L.B., 2023. Design of Zr-MOFs by introducing multiple ligands for efficient and selective capturing of Pb (II) from aqueous solutions. *ACS Appl. Mater. Interfaces* 15 (4), 5974–5989. <https://doi.org/10.1021/acsami.2c21546>.
- Liu, X., Tang, J.L., Fu, L.K., Wang, H., Wang, S., Xiong, C., Wang, S.X., Zhang, L.B., 2023. Ligand design of a novel metal-organic framework for selective capturing of Pb(II) from wastewater. *J. Clean. Prod.* 386, 135841. <https://doi.org/10.1016/j.jclepro.2022.135841>.
- Liu, Y.F., Ding, L.J., Yan, A., Wei, J.T., Liu, Y., Niu, Y.Z., Qu, R.J., 2024. Facile fabrication of UIO-66-NH<sub>2</sub> modified with dodecyl and polyethyleneimine by post-synthesis functionalization strategy and simultaneous adsorption removal of anionic and cationic dyes. *Colloids Surf. A Physicochem. Eng. Asp.* 692, 134019. <https://doi.org/10.1016/j.colsurfa.2024.134019>.
- Lv, X., Liu, Y., Zhang, J., Zhao, M., Zhu, K., 2019. Study on the adsorption behavior of glutaric acid modified Pb(II) imprinted chitosan-based composite membrane to Pb (II) in aqueous solution. *Mater. Lett.* 251, 172–175. <https://doi.org/10.1016/j.matlet.2019.04.101>.
- Mahmood, U., Alkorbi, A.S., Hussain, T., Nazir, A., Qadir, M.B., Khaliq, Z., Faheem, S., Jalalah, M., 2024. Adsorption of lead ions from wastewater using electrospun zeolite/MWCNT nanofibers: kinetics, thermodynamics and modeling study. *RSC Adv.* 14 (9), 5959–5974. <https://doi.org/10.1039/d3ra07720a>.
- Maleki, B., Baghayeri, M., Ghanei-Motlagh, M., Mohammadi Zonozi, F., Amiri, A., Hajizadeh, F., Hosseiniar, A., Esmaelnezhad, E., 2019. Polyamidoamine dendrimer functionalized iron oxide nanoparticles for simultaneous electrochemical detection of Pb<sup>2+</sup> and Cd<sup>2+</sup> ions in environmental waters. *Measurement* 140, 81–88. <https://doi.org/10.1016/j.measurement.2019.03.052>.
- Martinez-Haro, M., Green, A.J., Mateo, R., 2011. Effects of lead exposure on oxidative stress biomarkers and plasma biochemistry in waterbirds in the field. *Environ. Res.* 111 (4), 530–538. <https://doi.org/10.1016/j.envres.2011.02.012>.
- Mohammadi, A., Jafarpour, E., Mirzaei, K., Shoaiei, A., Jafarpour, P., Beikmohammadi Eyni, M., Mirzaei, S., Molavi, H., 2024. Novel ZIF-8/CNC Nanohybrid with an interconnected structure: toward a sustainable adsorbent for efficient removal of Cd (II) ions. *ACS Appl. Mater. Interfaces* 16 (3), 3862–3875. <https://doi.org/10.1021/acsami.3c15524>.
- Molavi, H., 2025. Cerium-based metal-organic frameworks: synthesis, properties, and applications. *Coord. Chem. Rev.* 527, 216405. <https://doi.org/10.1016/j.ccr.2024.216405>.
- Molavi, H., Salimi, M.S., 2025. Investigation the effect of exchange solvents on the adsorption performances of Ce-MOFs towards organic dyes. *Sci. Rep.* 15 (1), 7074. <https://doi.org/10.1038/s41598-025-90313-8>.
- Qiu, S.J., Wang, X., Zhang, Q.R., Nie, G.Z., 2022. Development of MoS<sub>2</sub>/cellulose aerogel nanocomposite with superior application capability for selective lead(II) capture. *Sep. Purif. Technol.* 284, 120275. <https://doi.org/10.1016/j.seppur.2021.120275>.
- Ren, X., Wang, C.-C., Li, Y., Wang, P., Gao, S., 2023. Defective SO<sub>3</sub>H-MIL-101(Cr) for capturing different cationic metal ions: performances and mechanisms. *J. Hazard Mater.* 445, 130552. <https://doi.org/10.1016/j.jhazmat.2022.130552>.
- Ruan, W., Liu, H., Wu, H., Qi, Y., Zhou, M., Zhou, C., Zhang, Z., Yang, H., 2022. Fabrication of Uio-66-NH<sub>2</sub> with 4,6-Diamino-2-mercaptopurimidine facilitate the removal of Pb<sup>2+</sup> in aqueous medium: nitrogen and sulfur act as the main adsorption sites. *Fuel Process. Technol.* 236, 107431. <https://doi.org/10.1016/j.fuproc.2022.107431>.
- Sgreccia, E., Rogalska, C., Gonzalez, F.S.G., Proposito, P., Burratti, L., Knauth, P., Di Vona, M.L., 2024. Heavy metal decontamination by ion exchange polymers for water purification: counterintuitive cation removal by an anion exchange polymer. *J. Mater. Sci.* 59 (7), 2776–2787. <https://doi.org/10.1007/s10853-024-09356-3>.
- Sun, C., Ji, Y., Bi, K., Tian, H., Wang, C., Deng, F., Zhang, Y., 2024. Tuning oxygen vacancy and missing linkers of defective MOF-808 for advanced adsorption of Yb(III) from aqueous solution. *Sep. Purif. Technol.* 347, 127585. <https://doi.org/10.1016/j.seppur.2024.127585>.

- Suryaprabha, T., Sethuraman, M.G., 2018. Fabrication of superhydrophobic and enhanced flame-retardant coatings over cotton fabric. *Cellulose* 25 (5), 3151–3161. <https://doi.org/10.1007/s10570-018-1757-8>.
- Tang, J., Chen, Y., Zhao, M., Wang, S., Zhang, L., 2021. Phenylthiosemicarbazide-functionalized UiO-66-NH<sub>2</sub> as highly efficient adsorbent for the selective removal of lead from aqueous solutions. *J. Hazard Mater.* 413, 125278. <https://doi.org/10.1016/j.jhazmat.2021.125278>.
- Wang, H., Wang, S., Wang, S., Tang, J., Chen, Y., Zhang, L., 2022. Adenosine-functionalized UiO-66-NH<sub>2</sub> to efficiently remove Pb(II) and Cr(VI) from aqueous solution: thermodynamics, kinetics and isothermal adsorption. *J. Hazard Mater.* 425, 127771. <https://doi.org/10.1016/j.jhazmat.2021.127771>.
- Wang, R., Shi, X., Wang, H., Lei, C., 2015. Novel Silica sorbents surface-functionalized with a Salicylyhydroxamic acid-based ion-imprinting polymer for the selective removal of Pb(II) from aqueous solution. *J. Chem. Eng. Data* 60 (5), 1454–1463. <https://doi.org/10.1021/je501158b>.
- Winiarska-Mieczan, A., 2018. Protective effect of tea against lead and cadmium-induced oxidative stress—a review. *Biometals* 31 (6), 909–926. <https://doi.org/10.1007/s10534-018-0153-z>.
- Wu, S.B., Ge, Y.J., Wang, Y.Q., Chen, X., Li, F.F., Xuan, H., Li, X., 2018. Adsorption of Cr (VI) on nano Uio-66-NH<sub>2</sub> MOFs in water. *Environ. Technol.* 39 (15), 1937–1948. <https://doi.org/10.1080/09593330.2017.1344732>.
- Xiang, D.W., Zhu, R., Chen, Y.F., Zhu, M.Y., Wang, S.X., Wu, Y.H., Luo, J.X., Fu, L.K., 2024. Preparation of amidoxime modified covalent organic framework for efficient adsorption of lead ions in aqueous solution. *Chem. Eng. J.* 492, 14. <https://doi.org/10.1016/j.cej.2024.152292>.
- Xie, Y.H., Guo, X.S., Wei, Y., Hu, H.Q., Yang, L.M., Xiao, H.J., Li, H.Y., He, G.H., Shao, P.H., Yang, G., Luo, X.B., 2024. Stable and antibacterial tannic acid-based covalent polymeric hydrogel for highly selective Pb<sup>2+</sup> recovery from lead-acid battery industrial wastewater. *J. Hazard Mater.* 479, 135654. <https://doi.org/10.1016/j.jhazmat.2024.135654>.
- Yang, Y., Li, J., Sheng, D., Ma, Q., Zhang, Y., 2023. Preparation of EDTA-modified UiO-66 for the selective removal of Cu(II) from water. *J. Solid State Chem.* 324, 124063. <https://doi.org/10.1016/j.jssc.2023.124063>.
- Yin, R., Liu, Y.H., Luo, Y., Yan, J., Li, J.L., Chen, D., Sun, T., Li, S.C., Wu, Z.J., 2025. Enhancing the liquid oxygen compatibility of epoxy resin by introducing a novel phosphorus/sulfur-containing flame retardant. *Polym. Degrad. Stabil.* 236, 12. <https://doi.org/10.1016/j.polymdegradstab.2025.111296>.
- Youness, F., Jaafar, A., Tehrani, A., Bilbeisi, R.A., 2022. Functionalised electrospun membranes (TETA-PVC) for the removal of lead(II) from water. *RSC Adv.* 12 (38), 24607–24613. <https://doi.org/10.1039/d2ra02946d>.
- Zhang, J., Li, T., Li, X., Liu, Y., Li, N., Wang, Y., Li, X., 2021. A key role of inner-cation-π interaction in adsorption of Pb(II) on carbon nanotubes: experimental and DFT studies. *J. Hazard Mater.* 412, 125187. <https://doi.org/10.1016/j.jhazmat.2021.125187>.
- Zhang, J., Wang, Z., Luo, Y., Zhang, Z., Feng, X., Zeng, Q., Tian, D., Li, C., Zhang, Y., Chen, S., 2023. Preparation and characterization of mercapto-functionalized calcined Attapulgite and its removal of Pb (II) and Cd (II) solution. *Minerals* 13 (10), 1337. <https://doi.org/10.3390/min13101337>.
- Zhang, Y., Guo, W., Liu, D., Ding, Y., 2023. Tuning the dual active sites of functionalized UiO-66 for selective adsorption of Yb(III). *ACS Appl. Mater. Interfaces* 15 (13), 17233–17244. <https://doi.org/10.1021/acsami.3c00938>.
- Zhang, Y., Liu, D., Guo, W., Ding, Y., 2022. Construction of novel nitrogen-rich covalent organic frameworks for highly efficient La(III) adsorption. *Sep. Purif. Technol.* 303, 122210. <https://doi.org/10.1016/j.seppur.2022.122210>.
- Zhang, Y., Sun, C., Ji, Y., Bi, K., Tian, H., Wang, B., 2024. Engineering linker-defects of MIL-101 series metal organic frameworks for boosted Yb(III) adsorption. *Sep. Purif. Technol.* 330, 125293. <https://doi.org/10.1016/j.seppur.2023.125293>.
- Zhao, M., Huang, Z., Wang, S., Zhang, L., Wang, C., 2020. Experimental and DFT study on the selective adsorption mechanism of Au(III) using amidinothiourea-functionalized UiO-66-NH<sub>2</sub>. *Microporous Mesoporous Mater.* 294, 109905. <https://doi.org/10.1016/j.micromeso.2019.109905>.
- Zhou, Q.Q., Yang, N., Li, Y.Z., Ren, B., Ding, X.H., Bian, H.L., Yao, X., 2020. Total concentrations and sources of heavy metal pollution in global river and lake water bodies from 1972 to 2017. *Global Ecology and Conservation* 22, 816. <https://doi.org/10.1016/j.gecco.2020.e00925>.
- Zhu, C., Hu, T., Tang, L., Zeng, G., Deng, Y., Lu, Y., Fang, S., Wang, J., Liu, Y., Yu, J., 2018. Highly efficient extraction of lead ions from smelting wastewater, slag and contaminated soil by two-dimensional montmorillonite-based surface ion imprinted polymer absorbent. *Chemosphere* 209, 246–257. <https://doi.org/10.1016/j.chemosphere.2018.06.105>.